SAND2015-1632C 96

Principal Component Analysis and study of port-induced swirl structures in a light-duty optical diesel engine

Author, co-author (Do NOT enter this information. It will be pulled from participant tab in MyTechZone)

Affiliation (Do NOT enter this information. It will be pulled from participant tab in MyTechZone)

Abstract

In this work computational and experimental approaches are combined to characterize in-cylinder flow structures and local flow field properties during operation of the Sandia 1.9L light-duty optical Diesel engine. A full computational model of the single-cylinder research engine was used that considers the complete intake and exhaust runners and plenums, as well as the adjustable throttling devices used in the experiments to obtain different swirl ratios. The in-cylinder flow predictions were validated against an extensive set of planar PIV measurements at different vertical locations in the combustion chamber for different swirl ratio configurations. Principal Component Analysis was used to characterize precession, tilting and eccentricity, and regional averages of the in-cylinder turbulence properties in the squish region and the piston bowl. Complete sweeps of the port throttle configurations were run to study their effects on the flow structure, together with their correlation with the swirl ratio. Significant deviations between the flows in the piston bowl and squish regions were observed. Piston bowl design, more than the swirl ratio, was identified to foster flow homogeneity between these two regions. Also, analysis of the port-induced flow showed that port geometry, more than different intake port mass flow ratios, can improve turbulence levels in-cylinder.

Introduction

The success of advanced, fuel-efficient and environmentally friendly combustion strategies for passenger vehicle engines is challenged by the need to meet regulatory emission mandates. Emissions are influenced by the details of the flow and combustion processes [1].

Flow structures in passenger-car light-duty Diesel engines are mostly defined by the port and piston bowl design, which are typically designed for conventional diesel combustion. The common geometric configuration with two different-shape ports, to generate in-cylinder swirl motion, and a piston bowl, aims at achieving a high bulk rotating motion to foster mixing of very rich regions of the fuel jet with the surrounding air [2]. But the role of these flows in combustion and pollutant formation is still not well understood.

Thus, the present study focused on in-cylinder swirling flow structures in the Sandia National Laboratories (SNL) single-cylinder light-duty diesel engine facility [3]. This engine features throttling devices in the intake runners, to create different in-cylinder swirl ratio conditions. In the last few years, a number of studies was conducted using this engine for understanding how low-temperature combustion strategies could be applied to a production engine, by analyzing the effects of different flow conditions, fuel compositions, injection timings on local mixture preparation, combustion and pollutant formation [3-8]. As also well summarized in [9], in light-duty engines the spray typically targets the piston bowl rim in order to partially deflect the fuel into the piston bowl, and partially into the squish volume. Mixtures that penetrate into the squish volume from the tip of the jet are seen remain into the squish volume, in rich (at the jet centerline) and lean (at the jet bounds) conditions. Lean mixture regions, formed from the tails of the fuel jets, penetrate less into the squish region. The discrepancy in conditions between the squish and the bowl regions eventually leads to partial oxidation products - carbon monoxide (CO) and unburned hydrocarbons, UHC, in the squish volume. In this work, a full computational model of the engine [10] is used together with Principal Component Analysis (PCA) to achieve a better understanding of its flows, in different regions of the combustion chamber.

PCA is a statistical tool for dimension reduction of large, multivariate datasets [11,12]. It extrapolates important information from the dataset by assuming that its points are correlated to each other, and by finding an optimal ‘point of view’ from which these correlations are best seen – i.e., by defining a set of orthogonal variables, called principal components, along which the dataset variances are maximized [13]. PCA works in an unsupervised way, by performing eigenvector analysis over the dataset’s covariance matrix [14,15], suitable for purposes of simplification, data reduction and classification, simplified modeling [16]. PCA has also been used to generate skeletal reaction mechanisms [17-19], or to identify low-dimensional manifolds in composition space [20,21]. As far as engine combustion is concerned, PCA has been traditionally used for control purposes [22-24], while internal flows are usually studied using proper orthogonal decomposition (POD) [25-27].

POD is a similar multi-variate statistical method that aims at decomposing a scalar or vector dataset (for example, the velocity field) into a sum of weighted and *linear* basis functions (named modes). When restricted to a finite dimensional case, POD can be seen as an extension of PCA [28]. In a typical engine application of POD, the first mode of a set of velocity fields corresponds to the ensemble-averaged field of the Reynolds decomposition; higher orders contain instead turbulence fluctuation modes. For this reason, POD is extremely useful for studying time-resolved phenomena such as engine cycle-to-cycle variations, and has also been used to analyze cyclic variations of PIV swirl measurements [29,30]. The present

choice of using PCA was motivated by the aim to study only ensemble-averaged flow parameters.

The study is structured as follows. First, the experimental facility and the numerical simulation methodologies are summarised. Then, validation of the in-cylinder flow predictions against particle image velocimetry (PIV) measurements is carried out at three in-cylinder swirl ratios, during the intake and compression strokes. Then, PCA and region-based combustion chamber partitioning parameters are defined, and used to identify major bulk flow and turbulence structures in the cylinder. Finally, the effects on these flow quantities of a swirl ratio sweep, performed by throttling either the helical or the tangential intake ports, are discussed.

Engine and experimental setup

The engine used for this study is the Sandia National Laboratories optical light-duty Diesel engine. The experimental setup features a single cylinder, modified from a production GM 1.9L light-duty engine [3-8]. A schematic of the experimental configuration is reported in Figure 1. The engine features optical access through fused silica windows, which are located at the top of the cylinder liner, as well as a fused silica piston, which retains the full geometric details of the production piston, including the bowl shape and the valve recesses on the piston surface. The only difference between the optical and the production piston is a wider and deeper crevice region, which was designed to allow imaging within the piston bowl, which slightly reduces the engine's effective compression ratio. A summary of the engine's main geometric parameters and the operating conditions used for this study are reported in Table 1.

Swirl plates. The in-cylinder swirl ratio can be arbitrarily adjusted through throttle plates which are fitted in each of the intake ports, allowing for effective swirl ratios ranging from about Rs = 1.5 up to about Rs = 5.5, depending on the adopted throttle configuration between the helical and the tangential port [32].

Figure 2 depicts the intake throttling device mounted for swirl flow control. Both throttle plates have the shape of the duct cross section, and are fastened on a semi-cylindrical stem.

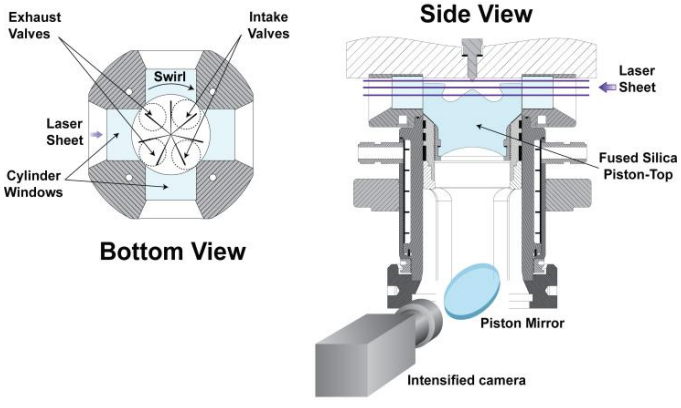

Fig. 1. Optical engine setup, including a schematic of the PIV measurement assembly.

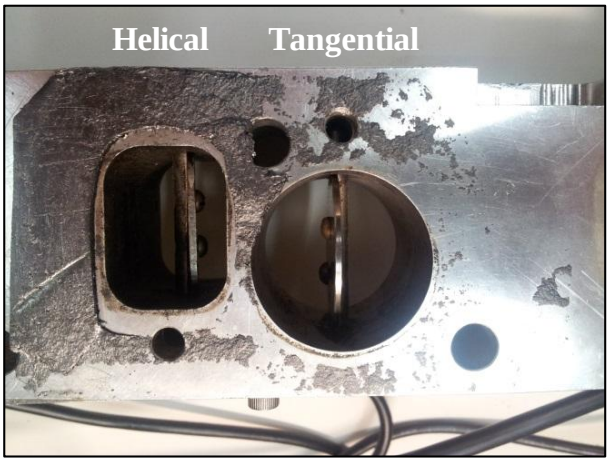

Figure 2. Intake throttling device, including details of the swirl plates.

Table 1. Engine and Experimental Setup details

Engine specifications

Bore x stroke [mm]	82.0 x 90.4
Unit displacement [cm^3]	477.2
Compression ratio	16.4 : 1
Squish height at TDC [mm]	0.88

Operating conditions

Intake charge composition	81% N_2, 10% O_2, 9% CO_2
Intake pressure [bar]	1.5
Intake temperature [K]	372.15
Engine speed [rpm]	1500
Swirl ratio [-]	1.5, 2.2, 3.5

A previous study [10,31] showed that most of the cylinder-bore-scale momentum in this engine enters the combustion chamber from the tangential port; thus, the highest swirl ratios can be achieved by letting this vortex enter the combustion chamber un-disturbed, by throttling the helical port almost up to its closure. On the other hand, throttling the tangential port leads to a non-uniform, yet monotone, decrease in bulk swirl ratio.

Furthermore, the same bulk swirl ratio values, when achieved using the different port throttling strategies, have been observed to yield significant differences in local flow field properties, especially in terms of the presence of vertical velocity components that lead to a less rigid vortex structure inside the cylinder. In particular, higher swirl ratios also led to very stable, almost rigid vortex structures, with negligible vertical components; instead, the lowest swirl ratios also showed noticeable presence of vertical mixing and a significant number of vertical streamlines all the way through the combustion chamber vertical span, especially in the central part, closer to the cylinder axis.

Both throttle devices are operated at 19 fixed pins that span the opening range from 0 (throttle closed) up to 90 degrees (wide-open throttle, WOT) in 5-degree incremental steps [32].

Experiments. PIV measurements of flow patterns during the intake and compression strokes were taken using porous SiO2 powder with

2 µm diameter, every 15 crank angle degrees during the intake and compression strokes [33]. Measurements were taken at three horizontal planes located at fixed distances from the fire-deck, namely dz = 3.0, 10.0, and 18.0 mm. Ensemble-averaged values were taken out of 150 sampled pairs, where the valid number of frames for each case was of 83 to 118, with a standard deviation of 25. A thorough description of the experimental procedure adopted for achieving the measurements is reported in [33,34].

Computational model.

A full engine computational model based on the KIVA code [35] was developed to reproduce the experimental results, and to explore flow structures where experimental measurements featured excessive distortion from the bowl-shaped optical piston assembly.

Geometry. In order to achieve maximum fidelity of the flow predictions, the combustion chamber, ports and valves, as well as the intake and exhaust runners and pressure-damping plenums, were modeled.

As reported in Figure 3, an unstructured, fully hexahedral mesh was developed. The mesh retains all piston and head geometric details, including valve cut-outs on the piston surface, valve recesses on the head, measured injector tip protrusion into the combustion chamber, as well as the liner crevice of the optical assembly. Wide usage was made of O-grid structures to guarantee that near-wall cells, especially at the liner and within the ports – across the valves where swirl flow develops –, were not excessively skewed or 'tent' shaped (i.e., sharing two adjacent faces with the wall surface), as seen in the view from the top in Figure 4.

Mesh refinement and improvements to the solver were introduced. In particular, the code was extended so that valve interiors could be modeled using an arbitrary number of cells. Also, the node movement algorithm was modified such that new cell layers – generated within the volume swept by the valve – matched the original mesh discretization. Mass flow predictions through the valves were converged when 27 cell layers were used to discretize the whole valve lift height (Figure 4, bottom), and the mesh discretization in this area featured thinner, high-resolution layers close to the valve seat. This allowed capturing the steep velocity gradients at valve opening/closing. A vertical resolution of 130µm was used. The squish region, which had 10 cell layers at TDC, achieved the same resolution as in previous sector mesh models [36].

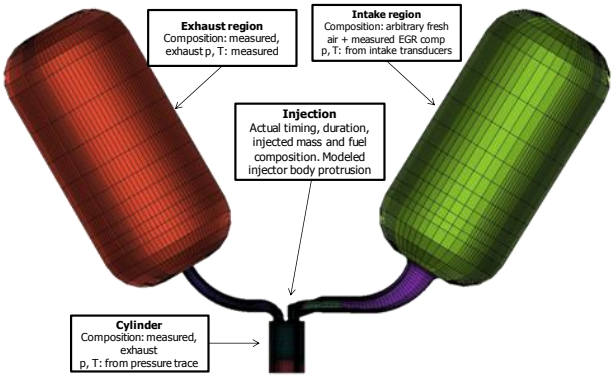

Figure 3. Overview of the computational domain.

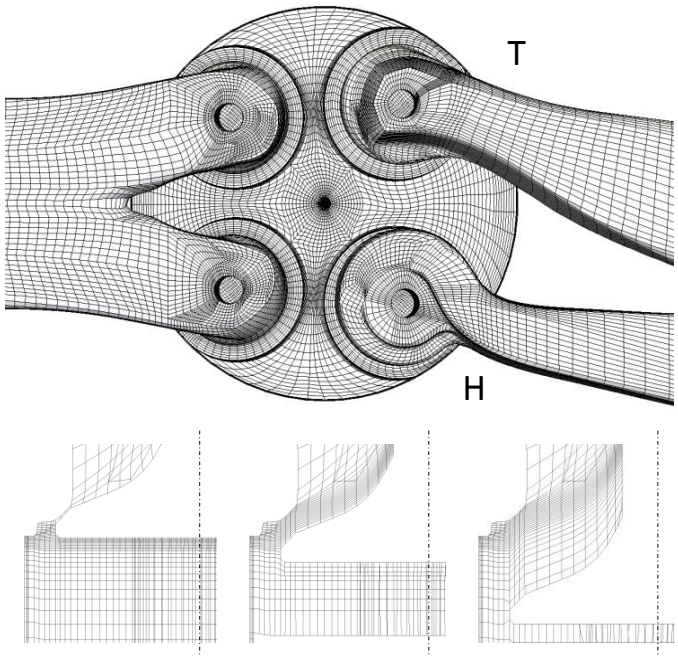

Figure 4. (top) Body-fitted cylinder and port grids as seen from the top over the cylinder head. (bottom) cross-sectional slices of the helical intake valve region when closed, partially open or at max lift.

In order to model the swirl plates in the intake runners, a mesh modification algorithm was used, as reported in [10] and shown in Figure 5. A layer of cells was de-activated to create a physical plate in the CFD model, and rotated up to the desired throttle angle. Node positions for a finite number of cell layers around the throttle plate were accordingly rezoned, so as to guarantee cell convexity and a good cell aspect ratio.

This set of computational grids provides good global swirl trends vs. variable throttle orientations [10] when compared with the steady-state flow bench measurements of [32], as well as with local tangential velocity profiles, and swirl center precession and tilting, during the compression stroke [37].

Table 2. Simulation parameters used for the present study.

Grid details

Mesh type	body-fitted hexahedral
Number of cells	682,091
Average cell size near TDC [mm]	0.7

Model details

Equations	Reynolds-Averaged Navier-Stokes
Solver	ALE (KIVA, Torres et al. [35])
Grid type	Unstructured, staggered
Turbulence	2-equation GRNG k-epsilon model, Wang et al. [38]
Chemistry solver	SpeedCHEM, Perini et al. [39,40]
Atomization	KH-RT, Beale and Reitz [41]
SGS near-nozzle flow field	Gas-jet, Abani and Reitz [42]
Law of the wall	Launder and Spalding [43]

Solver. The simulations were performed using the KIVA [35] Reynolds-Averaged Navier-Stokes (RANS) solver which allowed comparisons with the ensemble-averaged measurements.

The KIVA solver employs an Arbitrary Lagrangian-Eulerian method that at every time-step solves the (optional) spray and chemistry source terms, as well as the diffusion operators from a Lagrangian point of view, and then sub-cycles the advection terms explicitly, while moving the lagrangian node locations back to their physical positions. This procedure allows an intrinsically-mass-conserving arbitrary movement of the nodes during the simulation, anywhere within the domain. Turbulence was modeled using the GRNG two-equation k-epsilon model [38]. Thermo-physical properties were provided by the SpeedCHEM package [39,40], which makes use of the JANAF species tables. All major sub-models employed in the simulations are summarized in Table 2.

In order to minimize the effects of the previous-cycle residual flow field, each simulation was initialized at EVO (CA = 112 deg aTDC) using measured motoring pressure trace data at the end of the expansion stroke, and run for a whole cycle (720 CA degrees).

Results

Assessment of the flow field predictions

The accuracy of the predicted local flow field properties was tested using data from an extensive set of PIV measurements carried out at the Sandia Light-Duty optical diesel engine facility [34,47]. The experimental measurements were taken with three port configurations, which yield bench-equivalent swirl ratios of Rs = 1.5, 2.2, 3.5. These port setups mimic the ones used for swirl generation in a number of studies of partially-premixed combustion in the same engine [8,31-32,36 ,44]. Rs = 2.2 corresponds to the production engine swirl ratio (no intake throttles present). In this case, both throttles are in the fully-open position (WOT, wide-open throttle). Higher swirl ratios are achieved by throttling the helical port, such as the reference Rs = 3.5 case, where the throttle is at just 30 degrees aperture. Lower swirl ratios can be obtained through more complex port configurations. The reference Rs = 1.5 case was achieved by partially throttling both the helical and the tangential port using the same 70 degree throttle angle. A schematic representation of the computational meshes for the three reference port configurations is reported in Figure 5. PIV measurements in the experimental facility were taken every fifteen crank angle degrees during both the induction and the compression strokes for all three reference port configurations. Selected crank angle values – which show different flow properties – were chosen for comparing the model predictions with the experimental measurements, as reported in Figure 6.

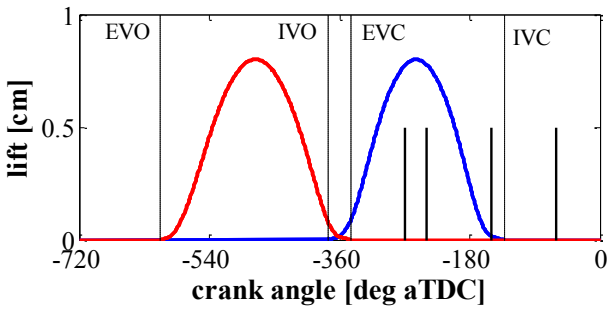

Figure 6. Valve lift profiles. Vertical lines represent model validation crank angles.

Intake stroke

As representative of the intake stroke, two crank angles close to the maximum intake valve lift, one during the ramp-up and one during the ramp-down portions of the valve movement were chosen. These conditions were challenging from both the experimental and modeling point of view. Strong background luminosity from the valve bottom surfaces made the PIV measurement result less reliable on the intake side of the cylinder. Furthermore, the valve bottoms are close to the measurement planes (less than 3 mm for the upper, dz = 10.0 mm plane), which makes the effects of the nearby wall boundary layer non-negligible.

Intake valve ramp-up. Figure 7 compares the PIV measurements and the simulation at the two lower planes. Data at dz = 3 mm from the fire-deck were not acquired due to physical interference of the valves with the laser sheet. Both Rs = 1.5 and 2.2 showed a similar swirl-plane flow structure with competing velocities entering from either intake valve. While the PIV images show a stronger effect of the helical port at Rs = 1.5, both datasets showed that flow entering from the tangential port has stronger horizontal/swirling components, whilst the helical port has almost radially-displaced horizontal components. This structure is noticeably different for Rs = 3.5, where the tangential port mass flow clearly overwhelms the helical port flow, up to having a not-yet rigid, but still quite definite, swirling vortex structure at both planes.

For all swirl ratios, the comparisons are clearer below the exhaust ports, where measurement errors are lower. Although the experimental images do not reach the liner, due to the piston geometry limiting the optical access, the same flow structure entering straight from the tangential port, hitting the liner and being deviated to form the incipient swirl vortex, was captured by the simulation.

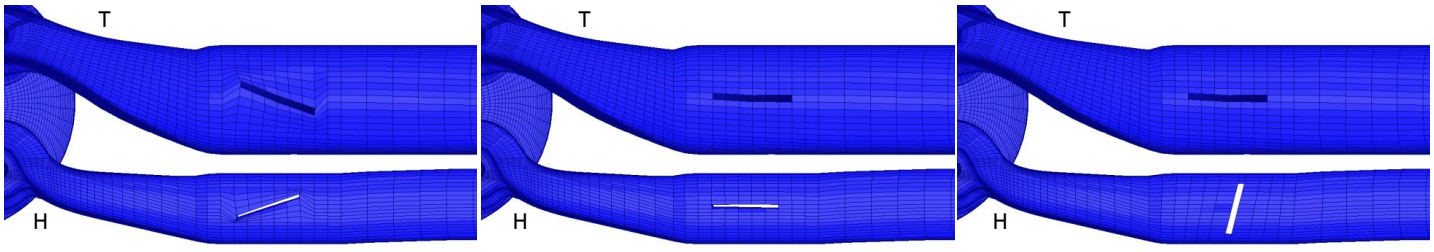

Rs = 1.5	H=15 (70°)	T=15 (70°)	Rs = 2.2	H=19 (90°)	T=19 (90°)	Rs = 3.5	H=6 (30°)	T=19 (90°)

Figure 5. Detail of swirl throttle pin positions at three reference swirl ratios: from the left, Rs = 1.5, 2.2, 3.5.

Intake valve ramp-down. Figure 8 shows the flow structures at the same planes about 30 crank angle degrees later, during the ramp-down part of the intake valve lift. At all swirl ratios, stronger velocity components are present, and momentum entered from the tangential port dominates the planar flow structure. At Rs = 1.5, due to it being partially throttled, some degree of competition with the helical port led to formation of recirculating flow regions (note that these competing components can be observed also in the experimental images, especially at dz = 10.0 mm).

At Rs = 3.5, the helical port is almost completely throttled, and momentum entering from the tangential port does not find any obstacles. In the center of the tangential port flow, smaller velocity components partially collapse into a recirculation bubble. This could be due to the flow having been split into two parts when crossing the valve stem. The formation of the wall boundary layer also makes the flow stream on the liner side weaker than at the center of the combustion chamber.

Compression stroke

Throughout the compression stroke the flow asymmetry introduced by the intake flow dissipates. Thus, flow predictions were compared first at -150 degrees aTDC, immediately before intake valve closure (IVC) where significant asymmetry in the flow field is still present; second, closer to TDC when the swirl vortex shows an almost rigid motion. The comparison is reported in Figures 9 to 11.

Compression, Rs = 1.5 (Figure 9). In this low-swirl-ratio case, the maximum horizontal velocity magnitudes are ~10 m/s, of the same order of the maximum piston velocity (7.1 m/s). This could make interference of the vertical velocity components in the time window of the PIV measurement potentially relevant.
In all planes and crank angles, the swirl center is consistently off-set towards the intake side of the combustion chamber. The simulation shows that, as time advances, the velocities at the liner have a clear precession/advancement motion.

Rs = 2.2 (Figure 10). In the baseline case, the maximum planar velocity magnitudes are approximately 50% larger than for Rs = 1.5: the comparison is more straightforward, and the overall swirl structure is already well-defined. At -150 degrees aTDC the strongest velocities are on the tangential port side of the combustion chamber. At -50 degrees aTDC both the simulation and the experiment show asymmetries at dz = 18.0 mm, where the proximity effects of the piston surface now start to be relevant.

Rs = 3.5 (Figure 11). At the largest swirl ratio, the swirl vortex is almost axisymmetric. Thus, similar projections are seen through the three planes. The swirl-center precession preserves what remains of the original intake flow complexity. The simulation captures this behavior too. At -150 degrees aTDC, all three planes show, consistently with the experiment, the swirl center to be located in the upper-right corner of the contour plots, i.e., in the helical port quadrant. At -60 deg aTDC the locations are slightly different depending on the plane, but still are consistently captured by the model: in the upper-left quadrant at dz = 3 mm; centrally located, below the exhaust valves at dz = 10.0 mm, centrally located, pointing towards the tangential port at dz = 18.0 mm.

Swirl structure study via Principal Component Analysis

The simulation results show that the swirl vortex structure in the engine changes significantly not only time-wise, as also seen from the PIV data, but also vertically space-wise, where even small changes in vertical coordinate (z) show both asymmetries and swirl centers following different paths. Thus, a set of tools was developed to process the simulation results, in order to obtain high-level data needed to extrapolate useful information to explain the swirl structure and its displacement within the cylinder.

Global swirl vortex structure

As Figure 12 shows, significant deviations can be also observed in terms of the planar swirl ratio, Rs_z. The planar swirl ratio was evaluated using the same definition as the global swirl ratio, where for each point on the plane, a mass corresponding to the mass of the momentum control volume corresponding to that same point [35] was used:

$$Rs\big|_{\Omega} = \frac{\sum_{i\in\Omega}\left[m_i(x_i - x_c)v_i - m_i(y_i - y_c)u_i\right]}{\omega\sum_{i\in\Omega}\left[m_i(x_i - x_c)^2 + m_i(y_i - y_c)^2\right]}, \qquad (1)$$

where ω represents the crank angle rotational speed, m_i and $\mathbf{x_i} = (x_i, y_i, z_i)$ the mass and position associated to each momentum node i in the point set Ω, and the coordinates of the center of mass $\mathbf{x_c} = (x_c, y_c, z_c)$ for the whole set were defined as:

$$\mathbf{x}_c\big|_{\Omega} = \frac{\sum_{i\in\Omega} m_i \mathbf{x_i}}{\sum_{i\in\Omega} m_i}. \qquad (2)$$

In the figure the planar results for dz = 3 mm show similar trends as from the corresponding measurements by Petersen and Miles [37]. Planar swirl ratios are seen to change significantly among the three planes. The discrepancies are wider as the piston approaches TDC: the dz = 10 mm plane has an almost steady swirl decay; the lowest plane, now into the bowl, shows the lowest swirl ratio values, while the uppermost plane has a high swirl ratio peak followed by a steep descent (note that because of background scattering from the valves, there is no experimental data in that interval).

The different swirl ratio trends indicate the need to study in-cylinder swirl on a local/regional basis. The whole combustion chamber domain was discretized using 20 equally-spaced horizontal planes for the squish region, and 5 equally-spaced planes for the piston bowl, in order to achieve a vertically-resolved representation of the swirl vortex structure that kept track of how the tangential velocities introduced by the intake flow propagate downwards in the combustion chamber and into the bowl.

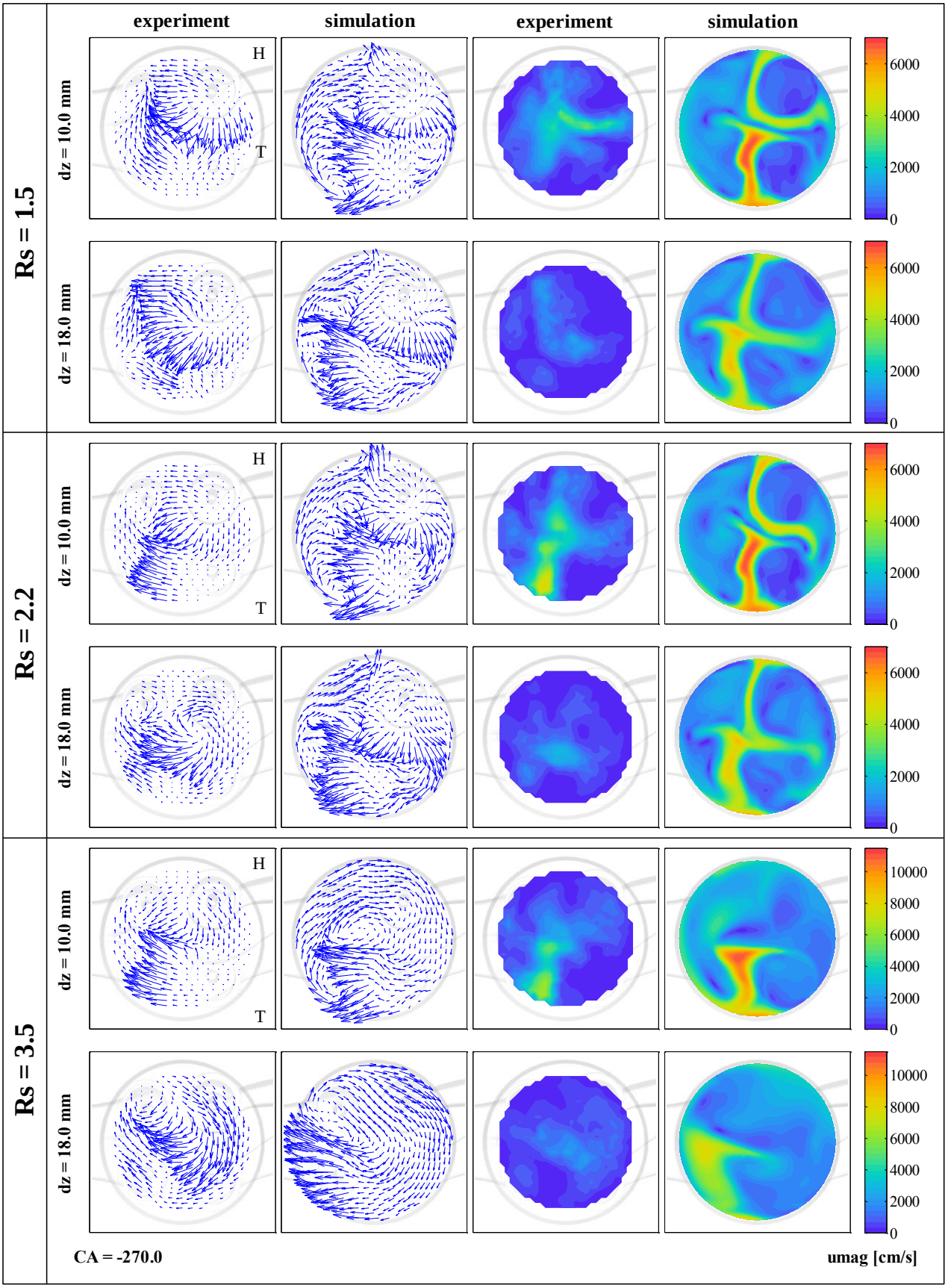

Figure 7. In-cylinder flow validation at CA = -270 degrees aTDC, during the induction stroke. Horizontal velocity components (left two columns) and velocity magnitudes (right two columns) at dz = 10.0 and 18.0 mm from fire-deck. Rs = 1.5 (rows 1-2), 2.2 (rows 3-4), 3.5 (rows 5-6).

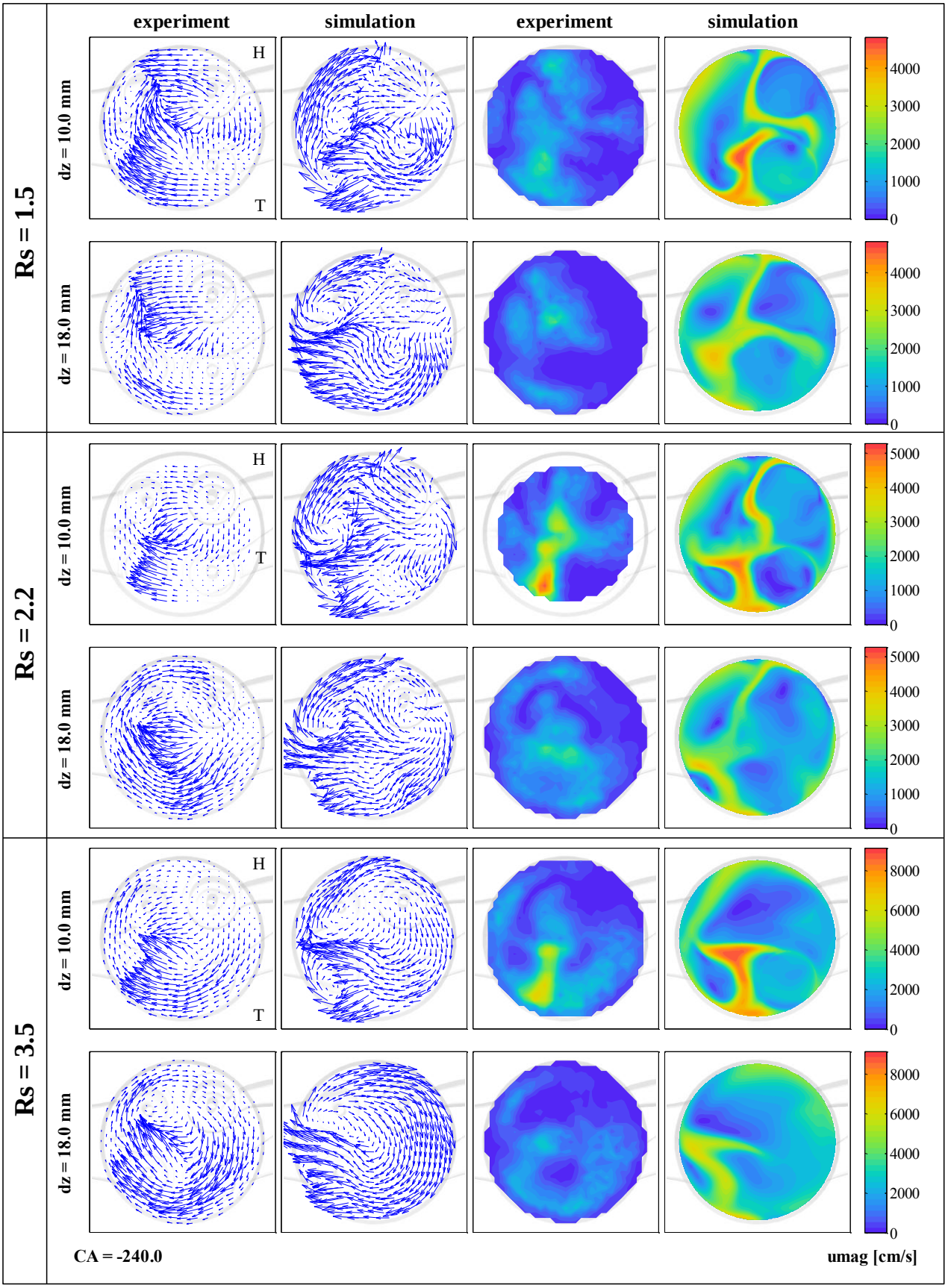

Figure 8. In-cylinder flow validation at CA = -240 degrees aTDC, during the induction stroke. Horizontal velocity components (left two columns) and velocity magnitudes (right two columns) at dz = 10.0 and 18.0 mm from fire-deck. Rs = 1.5 (rows 1-2), 2.2 (rows 3-4), 3.5 (rows 5-6).

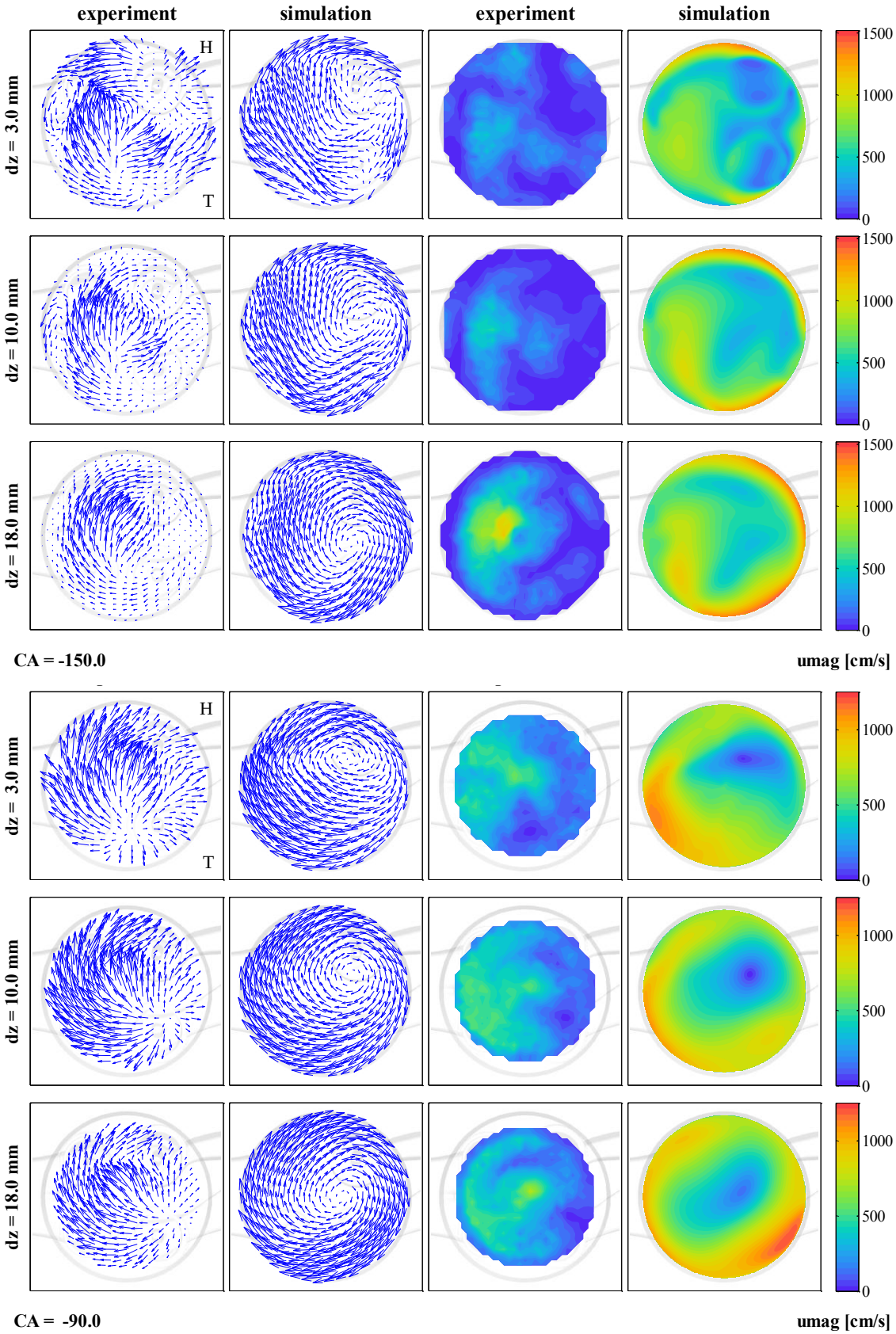

Figure 9. In-cylinder flow validation during the compression stroke, at Rs = 1.5. Horizontal velocity components (left two columns) and velocity magnitudes (right two columns) at dz = 3.0, 10.0 and 18.0 mm from fire-deck. CA = -150 (rows 1-3), -90 (rows 4-6) degrees aTDC.

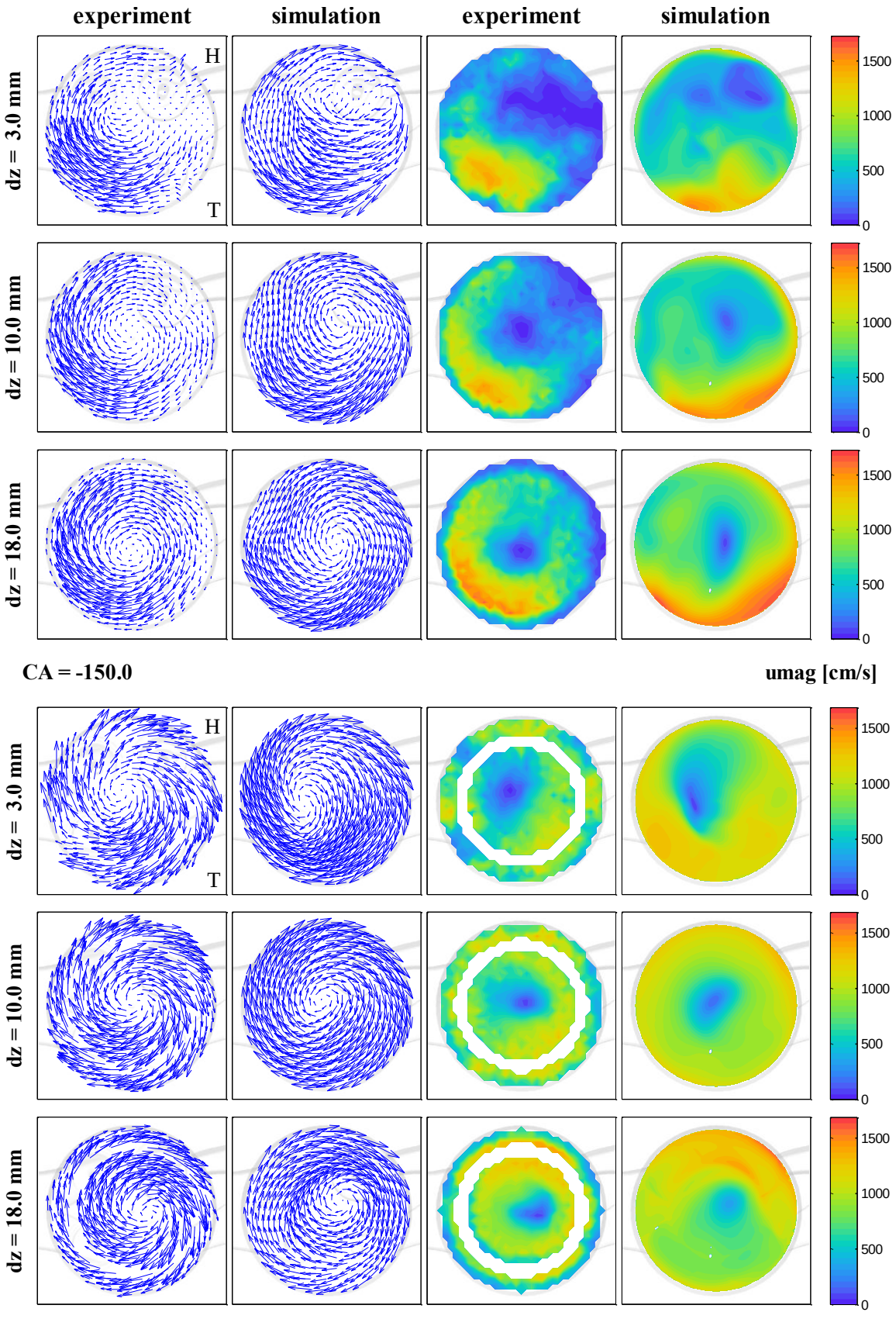

Figure 10. In-cylinder flow validation during the compression stroke, at Rs = 2.2. Horizontal velocity components (left two columns) and velocity magnitudes (right two columns) at dz = 3.0, 10.0 and 18.0 mm from fire-deck. CA = -150 (rows 1-3), -50 (rows 4-6) degrees aTDC.

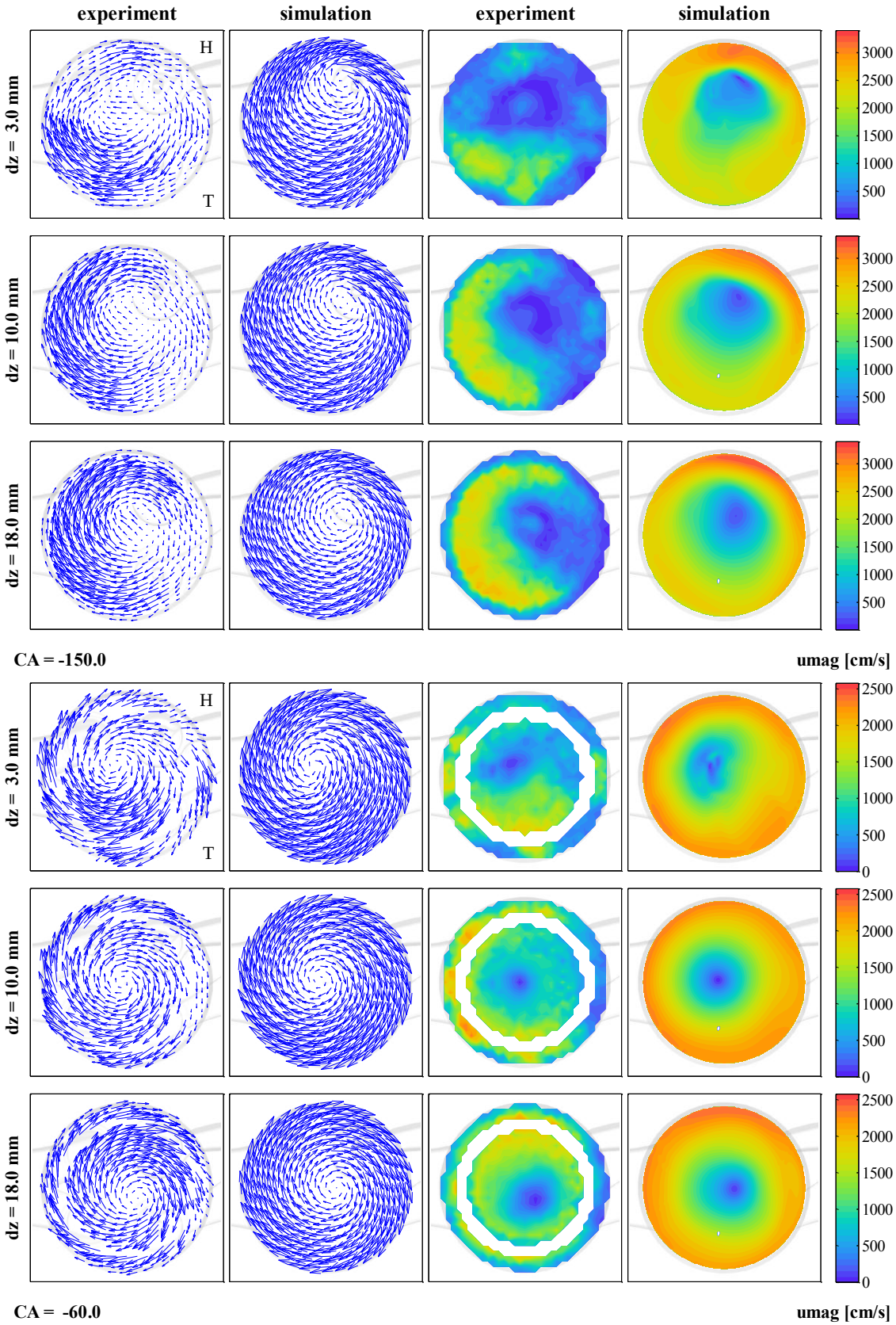

Figure 11. In-cylinder flow validation during the compression stroke, at Rs = 3.5. Horizontal velocity components (left two columns) and velocity magnitudes (right two columns) at dz = 3.0, 10.0 and 18.0 mm from fire-deck. CA = -150 (rows 1-3), -60 (rows 4-6) degrees aTDC.

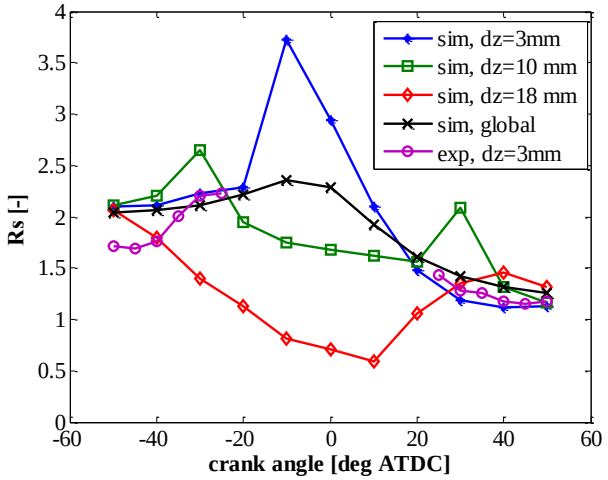

Figure 12. Comparison between global and planar swirl ratio values for the Rs=2.2 case, at the three PIV measurement planes: dz = 3.0, 10.0, 18.0 mm from the fire-deck. Experimental data at dz = 3.0 mm from [37].

Swirl center tracking. If the in-cylinder swirling vortex were a rigid body, the envelope of its planar swirl centers would be a straight vertical line. The predicted envelope of in-cylinder swirl centers, plotted using local planar swirl ratios as colors, is reported in Figure 13 at three port configurations and three different crank angles.

Late during the induction stroke (row 1, CA = -200 deg aTDC), an almost steady swirl center displacement was observed for all three swirl ratios. The lower part of the combustion chamber shows an almost linear structure, which is straighter the higher the swirl ratio – fostered by larger velocities entering from the tangential port. In the upper part of the combustion chamber and close to the valves there is a stronger eccentricity of the swirl centers. Rs = 3.5 shows a true step-like behavior due to strong velocities entering from the tangential port.

During the compression stroke (row 2, CA = -100 deg aTDC), most of these features are dissipated, and the swirl centers' envelope now resembles much more closely a straight line. Also the vertical swirl ratio distribution is much more homogeneous: as the squish volume is packed into a smaller vertical span, non-uniformities in the squish region are progressively attenuated. However, at this stage deviations between the piston bowl and the rest of the combustion chamber start to become significant: the overall swirl ratio in that volume remains noticeably lower and more eccentric.

This phenomenon is emphasized close to TDC (row 3, CA = -30 deg aTDC): the vertical swirl center displacement in the squish region is now a non-axisymmetric straight line, confirming that the effects of the in-cylinder non-uniformities are now concentrated into the specific non-axial displacement of the swirl centers. Despite the squish motion pushing charge into the piston bowl, the flow inside the bowl is still noticeably different in both overall swirl ratio and swirl center displacement.

Analysis of two different phenomena is needed to fully describe the swirl structure. First, convergence of the swirl centers to an almost straight line indicates a dimension reduction of the swirl vortex; second, the different flows in the squish vs. the bowl regions requires more analysis of the flow near TDC, since injection strategies for low-temperature combustion direct the fuel-air mixture into both regions [8].

Swirl vortex PCA

In order to study dimension reduction of the swirl vortex, Principal Component Analysis (PCA) [13] was employed. The first 'principal component' of the PCA is the direction along which the dataset shows maximum variance, while the second principal component is the direction with the second largest variance, and so on. The description of the analytical procedure behind PCA is explained in [20], and its Matlab implementation was used in the present study [21]. As a practical example, Figure 14 reports the two principal components for a generic two-dimensional scattered dataset, which resembles the shape of an ellipsoid. While PCA provides a set of eigenvectors of equal size to the dataset's dimensionality, selecting a smaller number of principal components allows one to simplify understanding of complex phenomena by only studying the behavior of their most significantly-varying quantities.

Reduced-dimensionality analysis was performed by running the PCA over the vertical swirl center locations, and then extracting the first principal component, which yields the main alignment direction. This provides the rotation axis the swirl vortex would have if it were a one-dimensional, perfectly rigid – yet non-axially aligned with the cylinder – body.

In order to describe the time-varying properties of the axis, the parameters represented in Figure 15 were used. The directional axis at the swirl vortex's center of mass is characterized in terms of its horizontal *eccentricity* (e) from the cylinder axis; the axis directions are represented as an *azimuthal angle* (ϑ), representing its precession, and an *elevation angle* (ϕ), measured from the vertical cylinder axis, representing tilt.

Regional swirl inhomogeneity

As seen in Figure 13, the swirl vortex structure is complex during the open-valve part of the intake stroke and towards the end of the compression stroke.

During the intake stroke non-uniformities are introduced by the strongly asymmetric flow in the upper part of the combustion chamber. The piston bowl appears to play a major role late during the compression stroke. During compression, flow acceleration only partially affects the fluid inside the piston bowl.

The simulation output was post-processed by separating the bowl region, including the piston crevice volume, and the squish region, as indicated in Figure 16.

Discussion

As a reference operating condition, the baseline Rs = 2.2 swirl ratio with both wide-open port throttles was chosen.

Flow properties. Figure 17 shows average bulk and turbulence properties, starting before intake valve opening (IVO) until after exhaust valve opening (EVO). Most of the *bulk swirl ratio* is provided by the flow in the squish region. Inside the bowl, the overall swirl is much lower throughout the whole open-intake-valve part of the cycle.

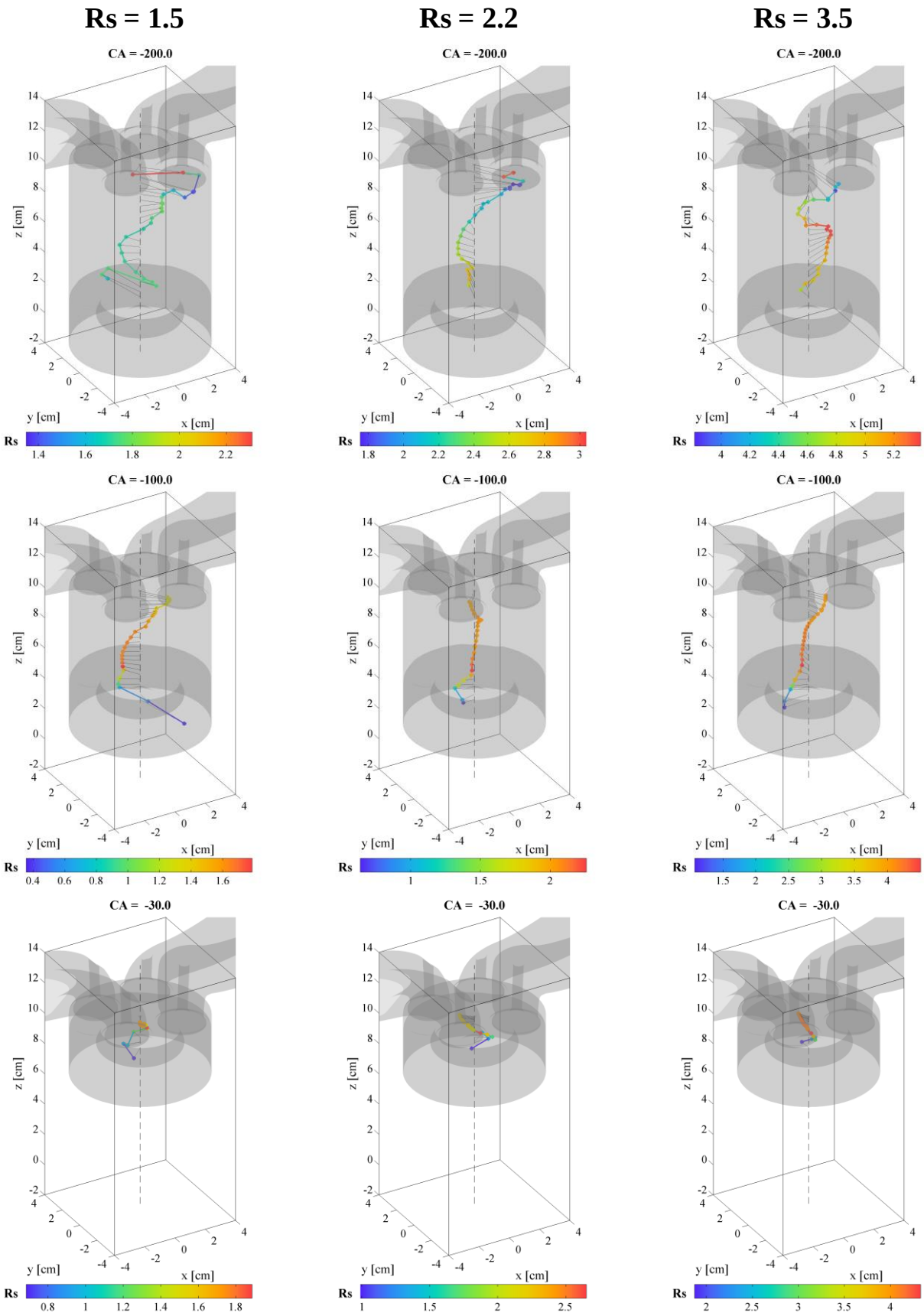

Figure 13. Vertical in-cylinder swirl center (points) and swirl ratio (colors) distribution at three reference port configurations. (row 1) intake flow, CA = -200 deg aTDC; (row 2) early compression flow, CA = -100 deg aTDC; (row 3) near-TDC late compression flow, CA = -30 deg aTDC.

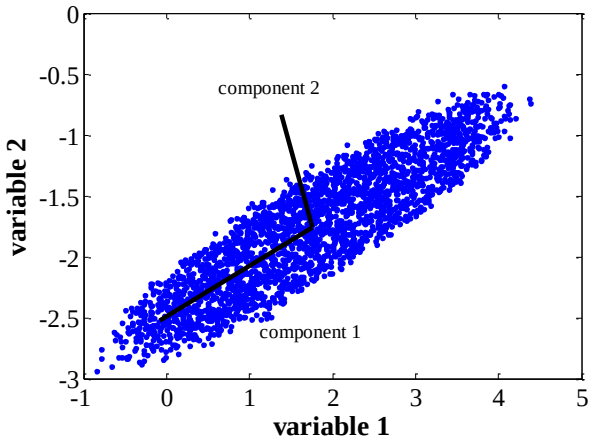

Figure 14. Example showing first two Principal Components extracted using PCA from a generic 2-dimensional sample dataset, which resembles the shape of an ellipsoid.

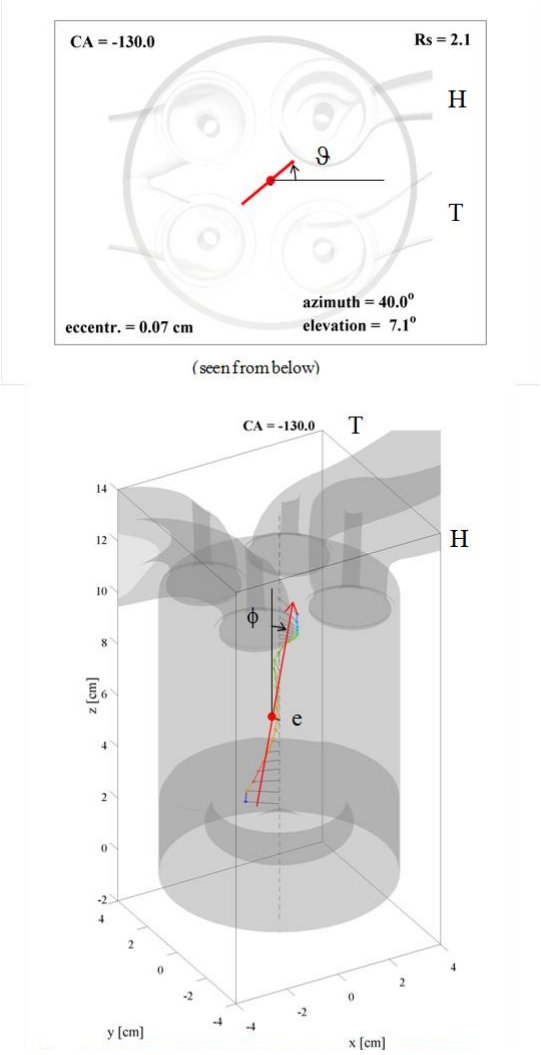

Figure 15. Schematic representation of the Principal Components in the swirl vortex motion: azimuthal angle (ϑ) and elevation (ϕ) of the vortex rotation axis; global swirl ratio (Rs) and eccentricity (*e*) of the vortex's center of mass.

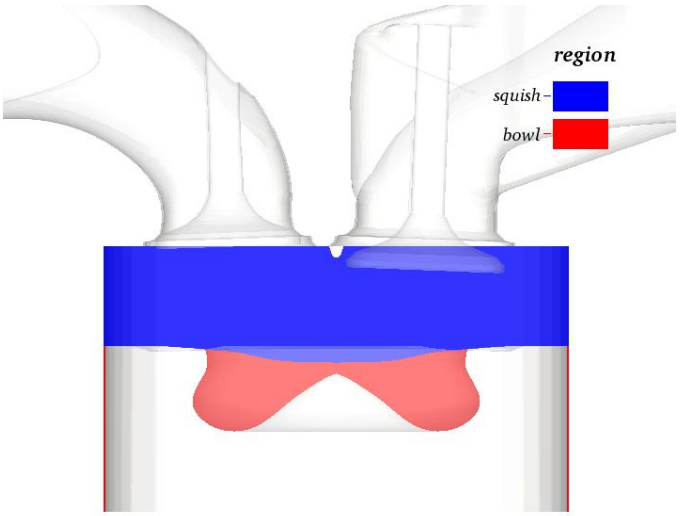

Figure 16. Region-based discretization of the combustion chamber.

However, the bowl swirl tends to increase to almost the same value as the squish swirl ratio near TDC when squish flow is significant, i.e., highly-swirling flow is pushed into the piston bowl, accelerating its swirling motion. This confirms that the charge in the bowl is well-mixed with the late-compression squish flow. For the same reason the swirl ratio inside the bowl remains larger after TDC during the expansion.

The *mass-averaged* turbulence intensity and length scale show specific regional behaviors as well. Despite the lower turbulence kinetic energy, the turbulence intensity within the bowl has the same order of magnitude as the squish level until the second half of the compression stroke. Then, squish flow entering the bowl introduces almost-orthogonal strain components, leading to a significant increase in turbulence intensity close to TDC. The squish region becomes very thin, and the two opposite wall boundary layers on the piston and head reduce the overall turbulence intensity in the squish region, so that ultimately the bowl is the region with stronger turbulence intensity at injection-like timings.

The modeled integral *turbulence length scale* (*L*) inside the bowl maintains a quasi-steady behavior of about 2 mm throughout the whole cycle. However, turbulence energy in the squish region is concentrated at smaller scales near TDC. This potentially explains the over-mixing observed in partially-premixed combustion experiments, where the major sources of unburned hydrocarbons and carbon monoxide arise in the squish region as a result of overly-lean fuel-air mixing near TDC [8].

PCA-swirl vortex behavior. Figure 18 reports the time-resolved behavior of the swirl vortex principal component, in terms of azimuthal (top), elevation (center) angle, and center-of-mass eccentricity (bottom), for both regions and the whole combustion chamber.

As far as *precessive motion* (azimuthal angle) is concerned, it was chosen not to constrain the angle value from 0 to 360 degrees, as the number of bounces across the bounds of the plot would have made it difficult to read. As already seen in two different PIV experiments [34,37], precessive motion in this engine is towards smaller angles, i.e., a counter-clockwise motion if observed from the piston bottom.

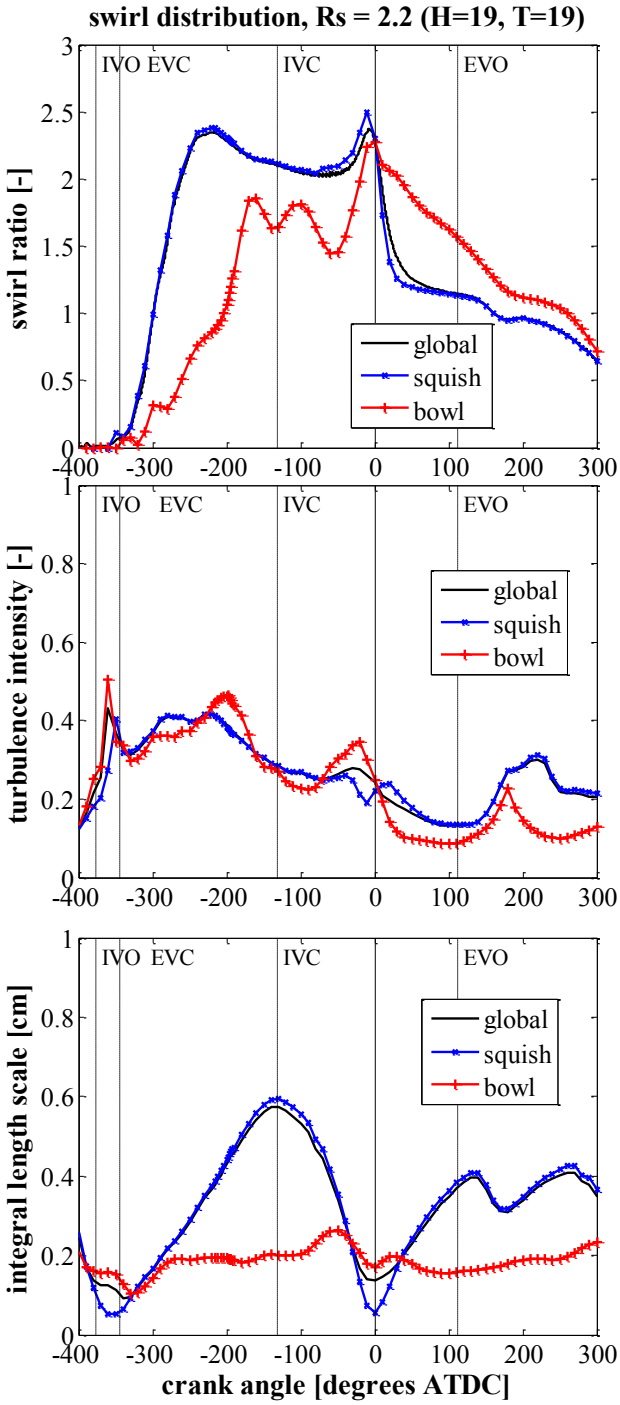

Figure 17. Regional averages of port-induced flow quantities: (top) swirl ratio, (center) turbulence intensity, (bottom) integral turbulence length scale. Squish and bowl region indicated in Figure 16.

An almost constant precession velocity is present throughout the cycle, apart from a limited crank-angle window between approximately -200 degrees aTDC and IVC. Until a 'developed' intake flow is present, the flow structure does not change much. After IVC, the bowl and squish behaviors start deviating significantly: precession continues in the squish region with approximately the same constant velocity, while it stops almost completely in the piston bowl, all the way to TDC.

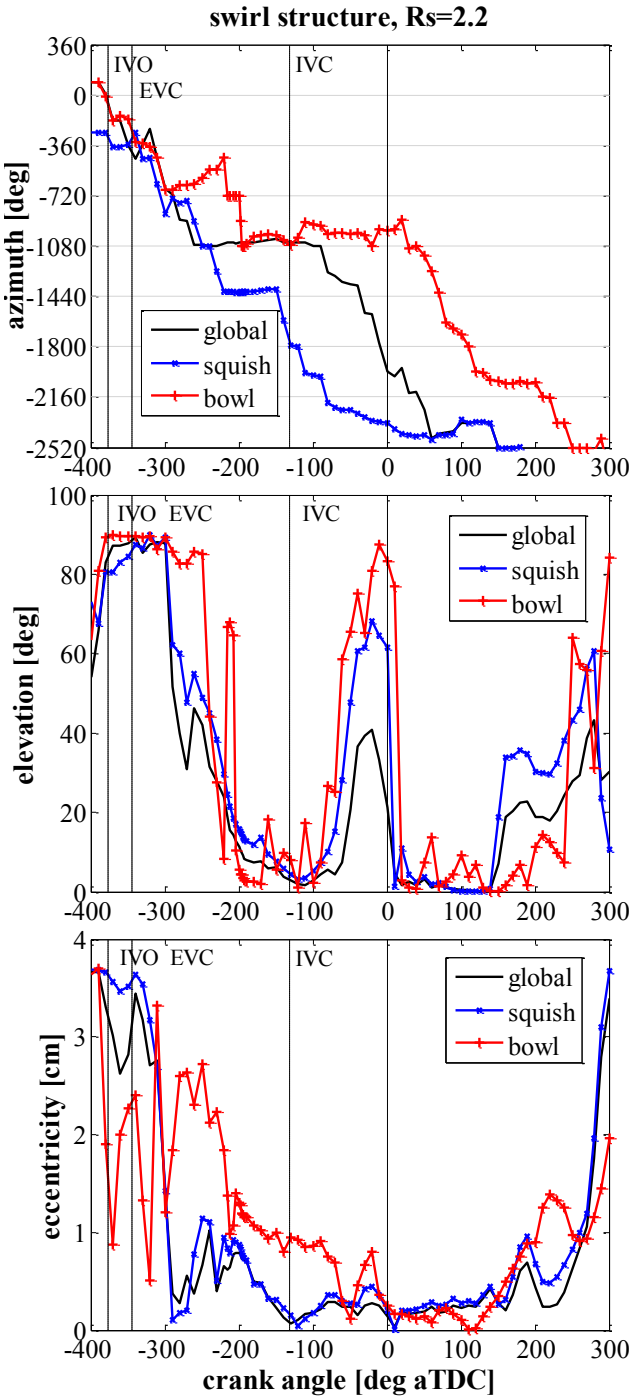

Figure 18. Regional averages of in-cylinder swirl structure: (top) swirl axis azimuthal orientation, (center) swirl axis elevation angle, (bottom) center of mass eccentricity. Squish and bowl region indicated in Figure 16.

The elevation angle and center-of-mass eccentricity measure how much the swirl vortex is *tilted*. Using the current definition (elevation as the angle between the swirl axis and the vertical axis), $\phi = 0$ corresponds to a perfectly vertical swirl vortex, and $\phi = \pi/2$ to a normal or tumble vortex. As Figure 18 shows, a stable vortex starts forming after -300 degrees aTDC – and even later in the bowl, after approximately -200 deg aTDC.

Due to the wide vertical span, swirl tilting is not very visible when the piston is close to BDC and the overall swirl vortex is almost vertical. However, momentum conservation increases the tilt as the squish region gets thinner, and a maximum tilt is seen a few degrees before TDC – again, at injection-like timing. Here, the squish and bowl regions have azimuthal angles on opposite sides of the combustion chamber. Thus, the globally averaged tilt angle is smaller than both, and not well representative of the amount of in-cylinder flow in-homogeneity.

The center-of-mass eccentricity increases during the first part of the induction stroke, also in the bowl region, where the piston is close to TDC. It dissipates almost completely during the compression stroke.

Port throttling study

For further analysis, different port configurations were studied. 'Near-TDC' averaged quantities were defined as time-averaged values over the crank angle interval from -50 degrees aTDC to top dead center, relevant to quantify flow properties at possible injection timings.

Two full single-port throttle sweeps were run, as reported in Figure 19. In each sweep one port was throttled up to a certain throttle angle, whilst the other port was kept wide-open. The simulation was then run for the same engine operating condition. Thus, a full mass-ratio sweep was achieved, from flow completely through the helical port, to flow completely through the tangential port. As can be seen, in the baseline configuration the engine has a mass flow ratio of 48.02 % through the tangential port.

Swirl ratio trends are reported in Figure 20. Both trends match bench-measured swirl ratio trends [10]. For all throttle configurations there is a consistent ratio between the bowl *Rs* and the squish *Rs*, even though they have different vortex structures and vertical velocity components.

Integral turbulence length scale sweeps, as in Figure 21, show that differences in average values are within ±20%, which is explained by the largest eddy sizes being constrained by geometric conditions.

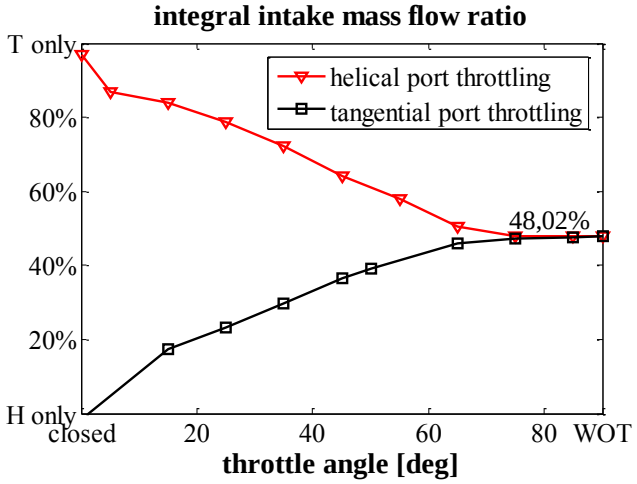

Figure 19. Integral port mass flow ratio versus throttle angle for helical/tangential port throttling configurations, with opposite port wide-open.

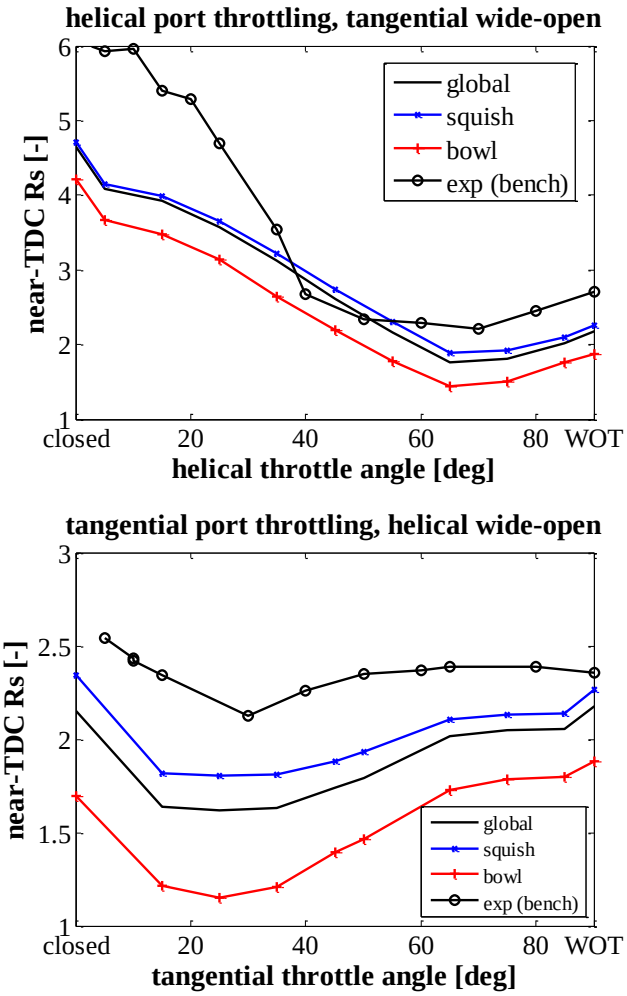

Figure 20. Regional near-TDC average swirl ratio trends for varying port throttling strategies. (top) helical port sweep, tangential wide-open; (bottom) tangential port sweep, helical wide-open.

Whatever the throttle configuration, the turbulent mixing scales in the squish region near TDC are smaller than in the bowl.

A strongly port-related quantity is the near-TDC turbulence intensity (I), as shown in Figure 22. Here, the trend is significantly asymmetric whether the helical, or the tangential port, is throttled. In the tangential throttle sweep, some slight increase in intensity is seen as the tangential port is closed. At the same time, the simulation predicts an almost constant near-TDC TKE for all tangential throttle configurations. This suggests that flow entering the combustion chamber through the tangential port has limited TKE. As this flow enters the cylinder, it takes the shape of a large-scale vortex, which implies limited dissipation into turbulence. Thus, reducing the inflow increases the turbulence intensity because the bulk velocities are reduced, not because of an increase in turbulence kinetic energy.

The turbulence intensity for varying helical port throttle angles is similar to the inverted near-TDC swirl ratio pattern of Figure 20. Flow entering from the helical port interacts with the large-scale vortex and introduces strain that generates smaller-scale eddies.

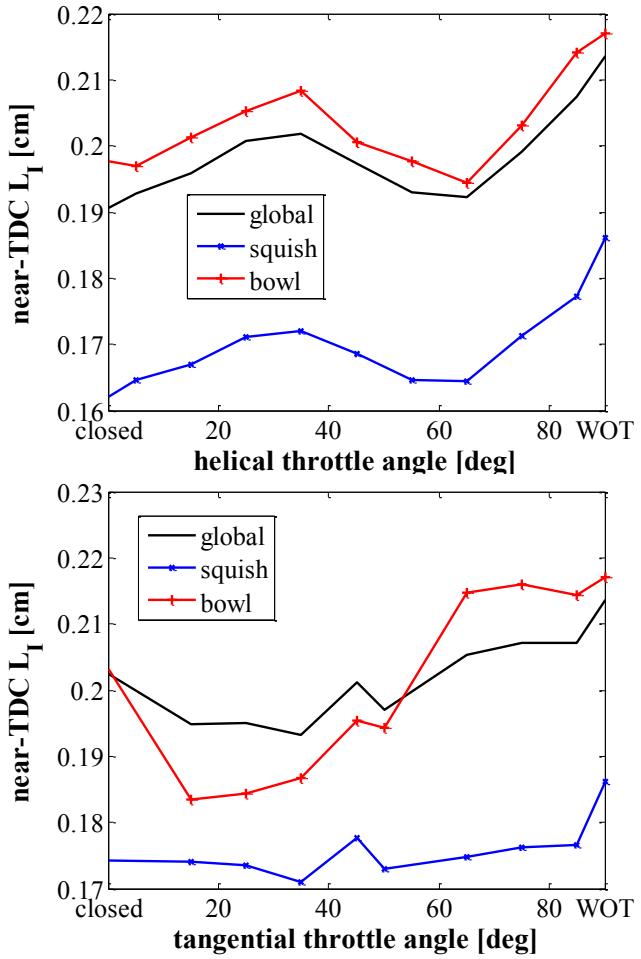

Figure 21. Predicted near-TDC average integral turbulence length scale trends for varying port throttling strategies. (top) helical port sweep, tangential wide-open; (bottom) tangential port sweep, helical wide-open.

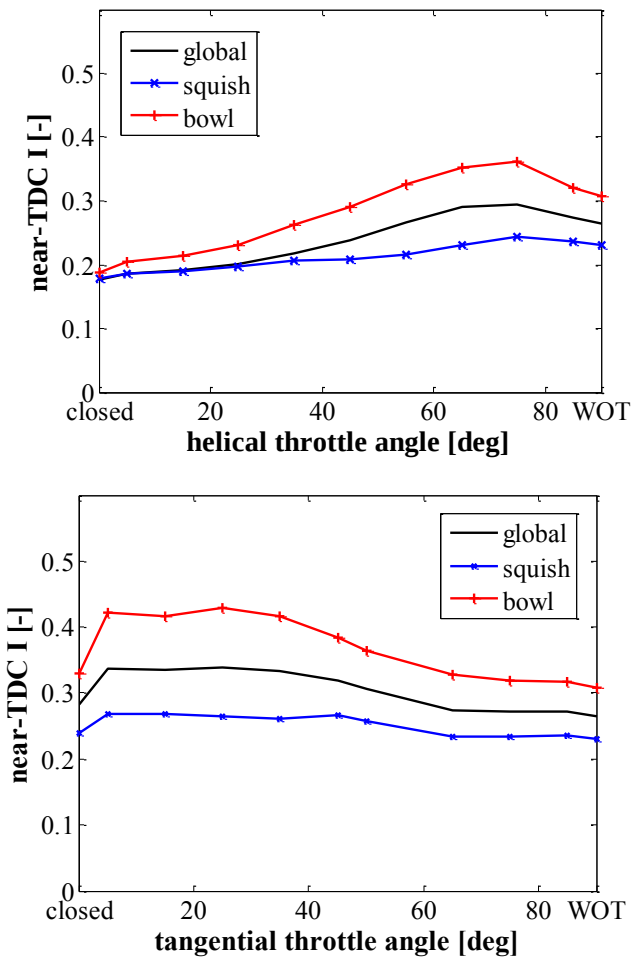

Figure 22. Predicted near-TDC average turbulence intensity trends for varying port throttling strategies. (top) helical port sweep, tangential wide-open; (bottom) tangential port sweep, helical wide-open.

Closing the helical port reduces the discrepancies in turbulence intensity between the two cylinder regions. This suggests that the vertical components induced by the helical port generate noticeably different turbulence intensities in the squish vs. the bowl region.

Finally, Figure 23 reports the near-TDC summary of the swirl-vortex's principal component representation for varying port configurations. As the swirl vortex exhibits precession, it is harder to draw universal considerations from this plot. However, two relevant phenomena can be observed. First, the limited effects of the tangential port sweep are seen also in terms of the principal components. Second, the flow complexity introduced by the helical port is confirmed by the PCA, and leads to complex trends of all three principal component quantities. Throttling the helical port not only reduces its mass flow, but also changes the flow direction.

These two behaviors suggest that helical port design can change the relationships between the bowl and squish bulk flows. The piston bowl shape should be considered as well, since less separation between the bowl and the rest of the cylinder helps render more homogeneous in-cylinder conditions [48].

Concluding Remarks

In this work a computational model of the Sandia light-duty optical diesel engine was validated against PIV measurements, and the in-cylinder swirl flow was characterized. The effects of different port-induced swirl configurations on turbulence were identified near-TDC using first principal component decomposition, as well as in region-averaged turbulence quantities.

A model validation was carried out at three different port configurations, with nominal swirl ratios Rs = 1.1, 2.2, 3.5. The model predictions were then used to study how flow field properties change in the squish and piston bowl volumes.

The Principal Component Analysis revealed time-resolved one-dimensional behavior of the in-cylinder swirl vortex, including its rotation axis, precession and tilt angles, as well as its center-of-mass eccentricity.

Finally, the tools were used to evaluate how the flow and turbulence properties change when either port is throttled.

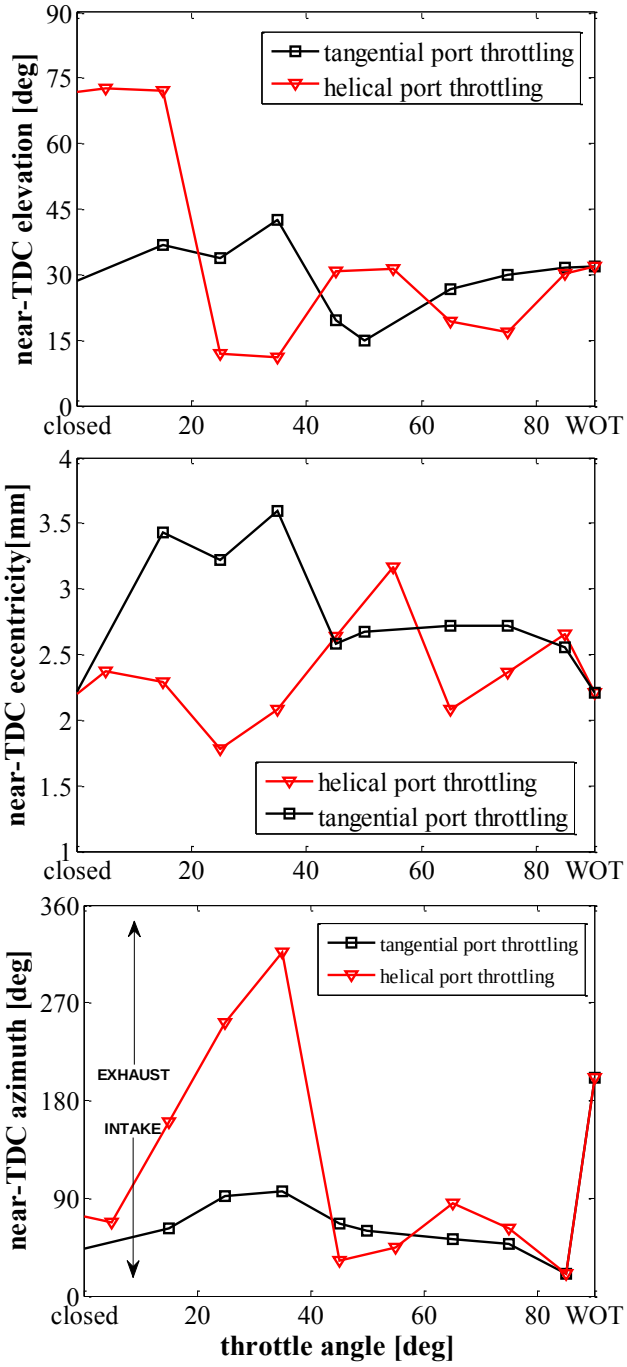

Figure 23. Near-TDC swirl vortex Principal Component trends for varying port throttling strategies. (top) elevation angle (center), eccentricity, (bottom) azimuth.

Based on this study, the following remarks were drawn:

- During the intake stroke, the incipient swirl structure is controlled by the port flow, and its status close to the valves is not representative of that in the main combustion chamber. Instead, it is very consistent later during the compression stroke (i.e., a near-rigid swirl vortex).
- The flow complexity is effectively represented by the one-dimensional principal component near TDC where non-axial behavior is enhanced by compression.
- Significant deviations in both bulk flow and turbulence quantities in the piston bowl versus in the squish region were seen: both turbulence and swirl levels in the bowl are smaller than in the squish region. Global average trends for the different port configurations are not sufficient to represent the in-cylinder flows in detail.
- Differences between the near-TDC bowl and the squish region flows remained similar when throttling the intake ports. This indicates that the charge in the bowl is mixed with the squish charge by the late-compression squish flow.
- Throttling the tangential port changes the swirl ratio significantly, but not the near-TDC turbulence. The tangential port generates a large-scale vortex that dissipates less into turbulence than the smaller-scale vortices from the helical port.
- Port throttling effects on the vortex principal components are complex. The tangential port introduces significant changes only in vortex eccentricity (linkable to the large-scale vortex structure); the helical port widely affects all components.

These results suggest that PCA analysis is useful for advanced port design and for describing different flow patterns.

References

1. Reitz RD, “Directions in internal combustion engine research”, Comb Flame 160(1), 1-8, 2013.
2. Heywood JB, “Fluid Motion Within the Cylinder of Internal Combustion Engines – The 1986 Freeman Scholar Lecture”, J. Fluids Eng. 109(1), 3-35, 1987.
3. Colban WF, Kim D, Miles PC, Oh S, Opat R, Krieger R, Foster D, Durrett R, Gonzalez MA, “A Detailed Comparison of Emissions and Combustion Performance Between Optical and Metal Single-Cylinder Diesel Engines at Low Temperature Combustion Conditions”, SAE technical paper 2008-01-1066, 2008.
4. Ekoto IW, Colban WF, Miles PC, Park SW, Foster DE, Reitz RD, Aronsson U, Andersson, O, “UHC and CO emissions Sources from a Light-Duty Diesel Engine Undergoing Dilution-Controlled Low-Temperature Combustion”, SAE technical paper 2009-24-0043, 2009, doi:10.4271/2009-24-0043.
5. Petersen BR, Ekoto IW, Miles PC, “An Investigation into the Effects of Fuel Properties and Engine Load on UHC and CO Emissions from a Light-Duty Optical Diesel Engine Operating in a Partially Premixed Combustion Regime”, SAE Int. J. Engines 3 (2010), 38-55. Doi:10.4271/2010-01-1470
6. Petersen BR, Sahoo D, Miles PC, “Review of Equivalence Ratio Measurements in a Light-Duty Diesel Engine Operating in a Light-Load Partially Premixed Regime”, THIESEL 2012 Conference on Thermo- and Fluid Dynamic Processes in Direct Injection Engines.
7. Sahoo D, Miles PC, Trost J, Leipertz A, “The Impact of Fuel Mass, Injection Pressure, Ambient Temperature, and Swirl Ratio on the Mixture Preparation of a Pilot Injection”, SAE Int. J. Engines 6(3):2013, doi:10.4271/2013-24-0061.
8. Sahoo D, Petersen B, Miles PC, “Measurement of Equivalence Ratio in a Light-Duty Low Temperature Combustion Diesel Engine by Planar Laser Induced

Fluorescence of a Fuel Tracer", SAE Int. J. Engines 4(2):2011,2312-2325, doi:10.4271/2011-24-0064.
9. Musculus MPB, Miles PC, Picket LM, "Conceptual models for partially premixed low-temperature diesel combustion", Progress in Energy and Combustion Science 39(2), 246-283, 2013.
10. Perini F, Miles PC, Reitz RD, "A comprehensive modeling study of in-cylinder fluid flows in a high-swirl, light-duty optical diesel engine", Computers & Fluids 2014(105):113-124, doi:10.1016/j.compfluid.2014.09.011.
11. Pearson K, "On lines and planes of closest fit to systems of points in space", Philosophical Magazine, 6(2), 559-572, 1901.
12. Hotelling H, "Analysis of a complex of statistical variables into principal components", Journal of Educational Psychology, 24, 417-441;498-520, 1933.
13. Jolliffe IT, "Principal Component Analysis (Springer Series in Statistics", 2nd edition, Springer, 2002. ISBN-978-0387954424.
14. Radhakrishna Rao C, "The Use and Interpretation of Principal Component Analysis in Applied Research", Sankhyā: The Indian Journal of Statistics, Series A (1961-2002), 26(4), 329-358, 1964.
15. Ding C, He X, "K-means Clustering via Principal Component Analysis", Proceedings of the 21st International Conference on Machine Learning, Banff, Canada, 2004.
16. Wold S, Esbensen K, Geladi P, "Principal Component Analysis", Chemometrics and Intelligent Laboratory Systems 2, 37-52, 1987.
17. Brown NJ, Li G, Koszykowski ML, " Mechanism Reduction via Principal Component Analysis", Int J Chem Kin 29(6), 393-414, 1997.
18. Vajda S, Valko P, Turanyi T, "Principal Component Analysis of Kinetic Models", Int J Chem Kin 17(1), 55-81, 1985.
19. Nagy T, Turanyi T, "Reduction of very large reaction mechanisms using methods based on simulation error minimization", Comb Flame 156, 417-428, 2009.
20. Sutherland JC, Parente A, "Combustion Modeling using principal component analysis", Proceedings of the Combustion Institute 32, 1563-1570, 2009.
21. Parente A, Sutherland JC, Tognotti L, Smith PJ, "Identification of low-dimensional manifolds in turbulent flames", Proceedings of the Combustion Institute 32, 1579-1586, 2009.
22. Albarbar A, Gu F, Ball AD, "Diesel engine fuel injection monitoring using acoustic measurements and independent component analysis", Measurement 43, 1376-1386, 2010.
23. Fog TL, Hansen LK, Larsen J, Hansen HS, Madsen LB, Sorensen P, Hansen ER, Pedersen PS, "On condition monitoring of exhaust valves in marine diesel engines", Neural Networks for Signal Processing IX, 1999. Proceedings of the 1999 IEEE Signal Processing Society Workshop, 554-563, 1999.
24. Wang X, Kruger U, Irwin GW, McCullough G, McDowell N, "Nonlinear PCA With the Local Approach for Diesel Engine Falut Detection and Diagnosis", IEEE Transactions on Control Systems Technology 16(1), 122-129, 2008.
25. Berkooz G, Holmes P, Lumley JL, "The proper orthogonal decomposition in the analysis of turbulent flows", Annu. Rev. Fluid Mech. 25, 539-575, 1993.
26. Chen H, Reuss DL, Sick V, "On the use and interpretation of proper orthogonal decomposition of in-cylinder engine flows", Meas. Sci. Technol 23(8), 085302, 2012.
27. Chen H, Reuss DL, Hung DLS, Sick V, "A practical guide for using proper orthogonal decomposition in engine research", Int J Engine Res 14(4), 307-319, 2013.
28. Kerschen G, Golinval J-C, Vakakis AF, Bergman LA, "The Method of Proper Orthogonal Decomposition for Dynamical Characterization and Order Reduction of Mechanical Systems: An Overview", Nonlinear Dynamics 41, 147-169, 2005.
29. Zhuang H, Hung DLS, Chen H, "Study of time-resolved vortex structure of in-cylinder engine flow fields using proper orthogonal decomposition technique", Proceedings of the ASME 2014 4th Joint US-European Fluids Engineering Division Summer Meeting, FEDMS2014, 2014.
30. Cosadia I, Borée J, Dumont P, "Coupling time-resolved PIV flow-fields and phase-invariant proper orthogonal decomposition for the description of the parameters space in a Diesel engine", Exp Fluids 43, 357-370, 2007.
31. Perini F, Zha K, Sahoo D, Busch S, Miles PC, Reitz RD, "Effects of in-cylinder non-uniformities on mixture preparation in a light-duty Diesel engine operating a light-load Partially Premixed Combustion strategy" - THIESEL 2014 Conference on Thermo- and Fluid Dynamic Processes in Direct Injection Engines, Valencia, Spain, 2014.
32. Opat RM, "Investigation of mixing and temperature effects on UHC/CO emissions for highly dilute low temperature combustion in a light-duty Diesel engine", M. S. Thesis, University of Wisconsin-Madison, 2006.
33. Zha K, Busch S, Miles PC, "Progress Towards In-Cylinder PIV Measurements throughout the Full Intake and Compression Strokes", Sandia National Laboratories technical report SAND 2014-3118P, 2014.
34. Zha K, Busch S, Miles PC, Wijeyakulasuriya S, Mitra S, Senecal PK, " Characterization of Flow Asymmetry During the Compression Stroke Using Swirl-Plane PIV in a Light-Duty Optical Diesel Engine with the Conventional Piston Bowl Geometry", SAE 2015 paper offer 15PFL-0808, 2015.
35. Torres DJ, Trujillo MF, "KIVA-4: An unstructured ALE code for compressible gas flow with sprays", Journal of Computational Physics 219(2):943-975, 2006.
36. Perini F, Dempsey AB, Reitz RD, Sahoo D, Petersen B, Miles PC, "A Computational Investigation of the Effects of Swirl Ratio and Injection Pressure on Mixture Preparation and Wall Heat Transfer in a Light-Duty Diesel Engine", SAE Technical Paper 2013-01-1105, SAE 2013 World Congress & Exhibition 2013, Detroit, MI, 2013.
37. Petersen B, Miles PC, "PIV Measurements in the Swirl-Plane of a Motored Light-Duty Diesel Engine", SAE Int. J. Engines 4 (2011) 1623-1641.
38. Wang B, Bergin M, Petersen B, Miles P, Reitz RD, Han Z, "Validation of the Generalized RNG Turbulence Model and Its Application to Flow in a HSDI Diesel Engine", SAE Technical Paper 2012-01-0140, 2012.
39. Perini F, Galligani E, Reitz RD, "An analytical Jacobian approach to sparse reaction kinetics for computationally efficient combustion modelling with large reaction mechanisms", Energy&Fuels 26 (8), 4804-4822, 2012.
40. Perini F, Galligani E, Reitz RD, "A study of direct and Krylov iterative solver techniques to approach linear scaling of the integration of Chemical Kinetics with detailed combustion mechanims", Combustion and Flame 161(5), 1180-1195, 2014.

41. Beale JC, Reitz RD, “Modeling spray atomization with the Kelvin-Helmholtz/Rayleigh-Taylor hybrid model”, Atomization and Sprays, 9(6), 1999:623-650.
42. Abani N and Reitz RD, “Unsteady turbulent round jets and vortex motion”, Physics of Fluids 19, 125102, 2007.
43. Launder BE, Spalding DB, “The numerical computation of turbulent flows”, Computer Methods in Applied Mechanics and Engineering 3(2), 269-289, 1974.
44. Sahoo D, Petersen B, Miles PC, “The impact of swirl ratio and injection pressure on fuel-air mixing in a light-duty diesel engine”, ASME ICES2012-81234, 2012.
45. Mathworks Inc., “Principal Component Analysis on data”, MATLAB R2009a documentation, http://www.mathworks.com/help/stats/princomp.html (accessed October 2014).
46. Hanson R, Curran S, Wagner R, Kokjohn S et al., “Piston Bowl Optimization for RCCI Combustion in a Light-Duty Multi-Cylinder Engine”, SAE Int. J. Engines 5(2):286-299, 2012, doi:10.4271/2012-01-0380.
47. Zha K, Perini F, Busch S, Park C, Reitz RD, Miles PC, “Experimental Investigation of Swirl Formation Process Using Swirl-Plane PIV in a Light-Duty Four-Valve Optical Diesel Engine,” JSAE/SAE 2015 Powertrains, Fuels & Lubricants International Meeting, 20159012, 2015, under review.

Definitions/Abbreviations

ALE	Arbitrary Lagrangian-Eulerian
aTDC	After Top Dead Center
bTDC	Before Top Dead Center
DERC	Direct injection Engine Research Consortium
EVC	Exhaust Valve Closing
EVO	Exhaust Valve Opening
I	Turbulence Intensity [-]
IVC	Intake Valve Closure
IVO	Intake Valve Opening
PCA	Principal Component Analysis
Rs	Swirl Ratio
RANS	Reynolds-Averaged Navier-Stokes
SGS	Sub-grid scale
SNL	Sandia National Laboratories
TDC	Top Dead Center
TKE	Turbulence kinetic energy [m^2/s^2]
WOT	Wide-open throttle

Contact Information

Federico Perini
Engine Research Center
University of Wisconsin-Madison
1015A Engineering Research Building
1500 Engineering Drive
Madison, WI 53706 (USA)
perini@wisc.edu

Acknowledgments

The authors wish to acknowledge support for this research by the Sandia National Laboratories under the U.S. Department of Energy, Office of Vehicle Technologies under contract DE-AC04-94AL85000, program managers Leo Breton, Gupreet Singh.